

Influence of Fe Underlayers on Stress Evolution of Ti in Ti/Fe  
Multilayers

Gregory B. Thompson – The University of Alabama  
Li Wan – The University of Alabama

Deposited 11/12/2018

Citation of published version:

Wan, L., Thompson, G. (2016): Influence of Fe Underlayers on Stress Evolution of Ti in Ti/Fe Multilayers. *Journal of Vacuum Science & Technology A*, 34(6).

DOI: <https://doi.org/10.1116/1.4962291>

# Influence of Fe underlayers on stress evolution of Ti in Ti/Fe multilayers

Li Wan and Gregory Thompson<sup>a)</sup>

Department of Metallurgical Engineering, The University of Alabama, Tuscaloosa, Alabama 35487-0202

(Received 12 June 2016; accepted 23 August 2016; published 7 September 2016)

A series of 40–2 nm bilayer spacing Ti/Fe multilayers were sputter-deposited. As the length scale of individual Ti layers equaled to 2 nm, Ti phase transforms from a hexagonal close packed (hcp)-to-body centered cubic (bcc) crystal structures for equal layer thicknesses in Ti/Fe multilayers. Further equal reductions in bilayer spacing to less than 1 nm resulted in an additional transformation from a crystalline to amorphous structure. Atom probe tomography reveals significant intermixing between layers which contributes to the observed phase transformations. Real-time, intrinsic growth stress measurements were also performed to relate the adatom mobility to these phase transformations. For the hcp Ti/bcc Fe multilayers of equivalent volume fractions, the multilayers undergo an overall tensile stress state to a compressive stress state with decreasing bilayer thickness for the multilayers. When the above phase transformations occurred, a modest reduction in the overall compressive stress of the multilayer was noted. Depending on the Fe thickness, the Ti growth was observed to be a tensile to compressive growth change to a purely compressive growth for thinner bilayer spacing. Fe retained a tensile growth stress regardless of the bilayer spacing studied. © 2016 American Vacuum Society. [<http://dx.doi.org/10.1116/1.4962291>]

## I. INTRODUCTION

Multilayered thin films with large surface area-to-volume ratios have been widely applied in magnetic devices,<sup>1,2</sup> semiconductors,<sup>3,4</sup> thermal coatings,<sup>5,6</sup> and optical filters.<sup>7,8</sup> As these multilayers individual layers are reduced in thickness, they can experience a change in phase. For example, in Co/Cr multilayers, Boher *et al.*<sup>9</sup> reported a change from hexagonal close packed (hcp) to body centered cubic (bcc) Co at  $\sim 15$  Å but later Vavra *et al.*<sup>10</sup> reported a bcc Cr phase transformed to hcp as the Cr thickness decreased 6 Å. Thompson *et al.*<sup>11,12</sup> reported in a Zr/Nb multilayered system where Zr can undergo a hcp to bcc phase change while Nb undergoes a bcc to hcp phase change. Thus, the criteria for the phase stability of multilayers, as a function of length scale, have resulted in considerable interest in what governs phase stability at these smaller length scales.

One approach in explaining phase stability in thin layers is associated with the strain changes induced by a phase transformation.<sup>13,14</sup> In this model, the film's transforming layer achieves a local energy minimum whose energy is higher than the bulk phase created by the strain of the lattice on a rigid substrate. As the volume of the film was reduced, via thinner layer thicknesses for fixed surface area, the material becomes more susceptible to such compliance induced strains that can drive a phase transformation. Another model specifically designed for two alternating bilayers in a multilayer is based on the competition between volumetric and interfacial energy changes between different structures.<sup>11,15–17</sup> When the layer thickness is sufficiently thin, or alternatively the volume reduced for a fixed surface area, the interfacial energy reduction for a phase change can dominate the volumetric energy penalty for such a phase transformation. From a thermodynamic prospective, the change in phase is placing the system

at its equilibrium condition considering the balance of the interfacial and volumetric energies. The strain contributions associated with a phase change can then be accommodated within the volumetric free energy term, with the chemical and strain contributions individual or collectively considered. Thompson *et al.* reported considered each contribution in the hcp to bcc transition of Zr for a series of Zr/Nb multilayers.<sup>11,12</sup> Other hcp to bcc transformations have also been reported for Ti in Ti/Nb multilayers.<sup>16,18</sup> In this system, the coherency strains were minimal as both  $\beta$ -Ti and bcc Nb have similar lattice parameters; however, a significant amount of Nb interdiffusion into the Ti layers was noted that contributed to a reduction in the volumetric energy penalty for the transformation. Consequently, this additional chemically intermixing stabilized the transformation to a larger layer thicknesses.<sup>16</sup> How strain and/or stress evolves in multilayers and regulates phase stability, either coherency strains at interfaces or chemical intermixing across interfaces is active in both the Ti/Nb and Zr/Nb systems. The role of stress evolution and its interrelationship to coherency strains, interface intermixing, and phase stability offers a rich area of scientific investigation.

Shull and Spaepn<sup>19</sup> were one of the earliest reports in the use of *in situ* wafer curvature studies capturing the growth stresses in a multilayered film. In this study, the growth behavior of Cu/Ag was investigated. Since both phases are face centered cubic (fcc), one would not expect a change in phase. Moreover, both metals are immiscible with respect to each other which would suggest a thermodynamic impedance to intermixing. Their results revealed a variation of both tensile and compressive stress evolution for a single layer as it grew on the other. Similar responses have also been noted in single films grown on rigid substrates. These stress states have been inferred to be related to the mobility of adatoms. It is generally accepted that initial compressive stress at the first stage of growth is a result of the atomic-scale migration into

<sup>a)</sup> Author to whom correspondence should be addressed; electronic mail: [gthompson@eng.ua.edu](mailto:gthompson@eng.ua.edu)

embryonic islands that form to minimize surface area to volumetric energies as the atoms nucleate on the substrate.<sup>20–22</sup> The subsequent tensile stress originates from the elastic strain associated with the coalescence of these islands to minimize the grain boundary energy. Upon postcoalescence of the grains, the stress may retain either a tensile or compressive state depending on the mobility of their adatoms.<sup>23–26</sup> Elemental films with low atomic mobility tend to retain the tensile condition with continued growth but films with atoms of higher intrinsic mobility will exhibit a return to compressive stress in the postcoalescence condition.<sup>27–30</sup>

The ability to measure, in real time, the stress response of a growing film offers opportunities to infer how phase stability may affect the evolving stress. In a recent paper by the authors,<sup>18</sup> it was noted that Ti initially grew with a tensile stress condition up to  $\sim 2$  nm, where upon it was compressive. Using postmortem analysis, Ti was stabilized up to  $\sim 2$  nm and the stress behavior was consistent with the type of tensile strains the bcc Ti would undergo to coherently match the bcc Nb subsurface. In this paper, we further studied to better understand how stress evolution is affected by both phases as well as the subsurface growth layer thickness. As noted previously in the coherence strain based models,<sup>13,14</sup> the change in phase was predicted for films on a rigid substrate (or growth surface). In a multilayer film, where the prior film deposited before the next layer is grown can be thin, its influence on the growth stress for the subsequent layer has not been extensively addressed. Unlike the prior Ti/Nb multilayer investigations,<sup>18</sup> Ti is the only species that known to have a bulk polymorph. In this investigation, we compare the growth stresses for Ti/Fe multilayers. Both species have known high temperature polymorphs— $\alpha$  hcp and  $\beta$  bcc Ti compared to  $\alpha$  bcc to  $\gamma$  fcc for Fe. This provides an interesting case study in determining which of these elemental films will transform, if at all, with reduction in layer thickness for equal layer thickness as well as how different layer thicknesses may change the growth stress of the thicker film.

## II. EXPERIMENT

The Ti/Fe multilayered thin films were sputter-deposited at equivalent individual layer thickness with bilayer thicknesses varying from 2 to 40 nm at ambient temperature ( $\sim 25^\circ\text{C}$ ) from  $>99.95\%$  pure elemental targets onto [001] Si substrates to a thickness of  $\sim 200$  nm. Additionally, two films with either 30 nm Ti/10 nm Fe and 10 nm Ti/30 nm Fe grown under the same sputtering conditions for a comparison that will be made more obvious once the experimental results are reported. The base vacuum pressure prior deposition was  $<10^{-8}$  Torr where upon ultrahigh purity Argon was flowed as the working gas at 10 standard cubic centimeters per minute to a pressure of 2 mTorr.

*In situ* stress evolution was monitored using *k*-Space Associates (kSA<sup>®</sup>) mutibeam optic sensor during the deposition process. The details about this laser interferometer technique can be found elsewhere.<sup>31</sup> Concisely stated the technique shines a laser pattern onto a substrate surface from which the reflective rays are captured and their relative

displacement measured as the substrate bends in response to the film's growth on the substrate. Using the Stoney's equation,<sup>32</sup> the amount of displacement is related to wafer curve and the stress in the film. The deposition rates of Ti and Fe were determined by dividing the film thickness, measured from x-ray reflectivity (XRR)<sup>33</sup> and confirmed by the transmission electron microscopy (TEM) cross-sectional micrographs, by the deposition time. XRR was performed on an X'pert Philips diffractometer operated with Cu  $K_\alpha$  radiation ( $\lambda = 1.5406 \text{ \AA}$ ) at 40 kV and 30 mA. The growth rates of Ti and Fe were found to be 0.029 and 0.053 nm/s, respectively.

A series of  $\theta$ - $2\theta$  scans of x-ray diffraction (XRD) was performed *ex situ* on a Bruker Discovery D8 general area diffraction detector systems with a Co  $K_\alpha$  radiation source operated at 40 kV and 35 mA for phase identification. Electron diffraction patterns were also taken in the plan-view orientation (normal to the substrate) in a FEI Tecnai F20 (S)TEM to further examine the phase constitutions of each multilayer. The plan-view foils were prepared by conventional TEM sample preparation method of cutting, polishing, dimpling and ion milling. Cross-sectional TEM foils were also imaged in the (S)TEM and they were prepared by a focused ion beam (FIB) lift out technique<sup>34</sup> followed by a 5 kV clean up step to reduce any  $\text{Ga}^+$  implantation into the foil. bright field images were taken to reveal the layered morphology of the multilayers with fast Fourier transformation from the higher magnification images were phase contrast imaging was evident to examine the orientation relationship between the two adjacent layers.

Finally, the multilayers were characterized by atom probe tomography (APT) performed in a Cameca Scientific Instruments Local Electrode Atom Probe (LEAP<sup>®</sup>) 3000XSi. The atom probe tips were prepared by a FIB lift out technique<sup>35</sup> and then sharpened into needlelike shapes with a 5 kV clean-up step to reduce any  $\text{Ga}^+$  implantation into the tip surface. The atom probe tips were analyzed at a base temperature of 40 K, 0.3 nJ laser pulse energy (wavelength 532 nm) at a repetition rate of 200 kHz in the laser mode.

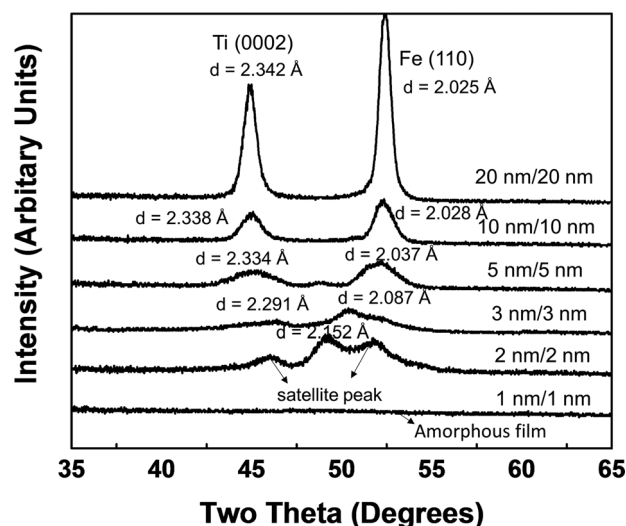


Fig. 1. XRD scans of Ti/Fe multilayers at various layer thicknesses.

TABLE I. Lattice strain in Ti/Fe multilayers calculated from XRD.

Layer thicknesses (nm/nm)	Ti				Fe		
	Ti 2 $\theta$ peak position (deg)	$d_{Ti}$ (Å)	Ti {0002} strain (%)	Ti {110} strain (%)	Fe 2 $\theta$ peak position (deg)	$d_{Fe}$ (Å)	Fe {110} strain (%)
20/20	44.91	2.342	0.00	N/A	52.41	2.025	0.00
10/10	44.99	2.338	-0.17	N/A	52.33	2.028	0.15
5/5	45.07	2.334	-0.34	N/A	52.11	2.037	0.59
3/3	46.90	2.291	-2.23	N/A	51.42	2.087	2.97
2/2	49.12	2.152	-8.83	-8.64	49.12	2.152	5.91
1/1	N/A	N/A	N/A	N/A	N/A	N/A	N/A

The reconstruction of the data was performed on IVAS 3.6.8 software following the procedures in Ref. 36.

### III. RESULTS AND DISCUSSION

Figure 1 shows the XRD scans of Ti/Fe multilayers at different equal bilayer thicknesses. It was observed that when the bilayer thickness is equaled or was larger than 6 nm (i.e., 20 nm/20 nm, 10 nm/10 nm, 5 nm/5 nm, and 3 nm/3 nm multilayers), both the {110} Fe peak at 52.41° and {0002} Ti peak at 44.91° were present in the scans. When the bilayer thickness decreased to 4 nm (or the 2 nm/2 nm multilayer), a single phase peak with satellite peaks resulting from the periodic stacking of the layers appeared. When the two separate phase peaks are present, as the bilayer thickness is reduced, these two major material peaks shift closer to each other indicative of lattice straining at the interface between the two phases. These peaks were fitted to a Gaussian profile where upon the 2 $\theta$  value was measured and converted to its d-spacing using Bragg's law. The change in d-spacing, or strain, was calculated using Eq. (1) where the 20 nm/20 nm multilayer was used as the reference value.

$$\varepsilon = \frac{d_1 - d_0}{d_1} \times 100\%, \quad (1)$$

where  $\varepsilon$  is strains,  $d_1$  is the calculated the lattice spacing from the peak position, and  $d_0$  is the referenced lattice spacing obtained from the 20 nm/20 nm multilayer.

The Ti peak shift to a higher angle indicates a compressive stress response while the Fe peak shift yields an ever increasing tensile strain with decreasing bilayer spacing (Table I). The strain values are relatively equivalent between the layers which would agree that each of these materials have similar elastic modulus values.<sup>37,38</sup> For the single phase peak noted for the 2 nm/2 nm multilayer, it is unclear which phase(s) this multilayer may have adopted since its peak position is not directly associated with either bulk phase. Furthermore, any determination at this point would be inconclusive from a single reflection. As will be discussed below, electron diffraction provided a complementary means to achieve phase identification. Finally, the 1 nm/1 nm multilayer did not reveal any noticeable crystallographic peaks in the XRD scan. As with the 2 nm/2 nm multilayer, electron diffraction again will provided assistance in the confirmation of the phase.

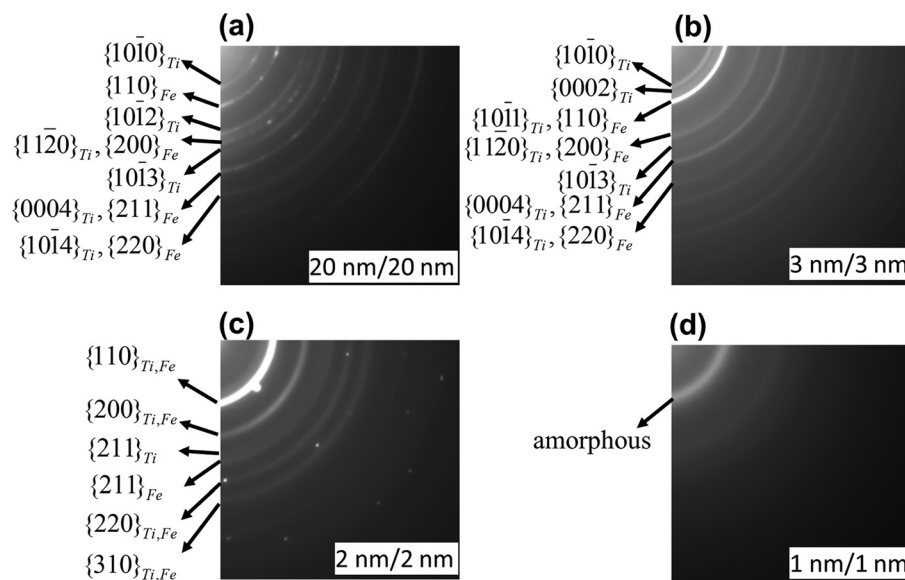


FIG. 2. (a) Electron diffraction pattern of 20 nm/20 nm Ti/Fe multilayer. The distinctive hcp Ti rings were shown. (b) Electron diffraction pattern of 3 nm/3 nm Ti/Fe multilayer. Distinctive hcp Ti reflections have confirmed that this film maintained hcp/bcc phases. (c) Electron diffraction pattern of 2 nm/2 nm Ti/Fe multilayer. Only bcc reflections were observed. (d) Electron diffraction of 1 nm/1 nm Ti/Fe multilayer. This pattern showed a typical amorphous structure.

Figures 2(a)–2(d) are electron diffraction patterns from the 20 nm/20 nm, 3 nm/3 nm, 2 nm/2 nm, 1 nm/1 nm Ti/Fe multilayers in the in-plane orientation. In Fig. 2(a), the first two rings were indexed as hcp Ti  $\{10\bar{1}0\}$  and bcc Fe  $\{110\}$  and the measured d-spacings from these patterns are close to their nominal lattice spacing 2.55 and 2.03 Å, respectively. This indicates, as did the XRD, both Ti and Fe are their bulk equilibrium phases and that neither film is experience significant strain while in contact with each other at these thicknesses. Since the Ti film is highly fiber textured along the closed packed (0001) planes, the  $\{0002\}$  reflection is not evident since the electron beam is parallel to this direction. In contrast, the multiple cubic variants for  $\{110\}$  could satisfy the diffraction condition and are seen in Fig. 2(a). Figure 2(b) shows the diffraction pattern for the 3 nm/3 nm multilayer. The brightest ring is indexed as hcp  $\{10\bar{1}1\}_{\text{Ti}}$  and bcc  $\{110\}_{\text{Fe}}$ , which is very broad. This broadening of the diffraction ring is attributed to a spread of the d-spacings that could be occurring as this Fe layer attempts to accommodate the hcp Ti interface. The measured d spacing is  $\sim 2.04$  Å and close to that of  $\{110\}$  Fe and relatively further from the  $\beta$ -Ti 2.33 Å for the same reflection. The distinctive hcp rings in Fig. 2(b) also suggest that the Ti layer has retained the bulk phase. As the thickness decreased to 2 nm/2 nm, the prior distinctive hcp reflections are not present and a single series of reflections that can be consistently indexed to a bcc phase is shown in Fig. 2(c). The lattice pattern of the first ring,  $a = 2.160$ , would match an equivalent lattice parameter for a  $\{110\}$  reflection for the single phase peak noted in the XRD scan of Fig. 1. Thus, combining the x-ray and electron diffraction, we have confirmed that Ti has undergone a hcp to bcc transition for this bilayer thickness.

It is worthy to note that a bcc TiFe intermetallic is known to exist;<sup>39</sup> however, no superlattice reflections were found suggesting that this was separate bcc phases in each layer. Figure 3(a) is a cross-sectional image of this multilayer along with an atom probe tomography compositional profile, Fig. 3(b). From these images, it is clear a multilayered structure is present, and not a single solid solution film. Each ring in the 2 nm/2 nm diffraction pattern, Fig. 2(c), is broad and can be attributed to the large strain created by the large lattice mismatch ( $\sim 13\%$ ) between the individual bcc Ti and Fe as well as the mixing of each species within each other's layer. Since Fe also has a possible option to undergo a polymorphic change, the presence of bcc Ti suggests that it is more favorable at these lower length scales. This is in agreement that the volumetric energy penalty for Ti hcp-to-bcc being modestly lower than that of Fe bcc-to-fcc, i.e.,  $\Delta G_{\text{hcp/bcc}}(\text{Ti}) = 4.57 \times 10^8 \text{ J/m}^3$  versus  $\Delta G_{\text{bcc/fcc}}(\text{Fe}) = 7.59 \times 10^8 \text{ J/m}^3$ .

For the 1 nm/1 nm thickness, the electron diffraction confirmed an amorphous ring, Fig. 2(d), and would be consistent with the lack of XRD reflections. The TEM cross-sectional images, Figs. 3(c) and 3(d), also confirm a microstructure with a lack of any crystallinity. Interestingly, the atom probe compositional profile, Fig. 3(e), does reveal the presence of a compositional modulations but whose intermixing is even larger than the prior 2 nm/2 nm profile in Fig. 3(b). The

vitrification between Ti and Fe alloys has been reported by others<sup>40–43</sup> with Guo<sup>43</sup> reporting that amorphous phases are formed when the atomic size difference are large and the mixing enthalpy is largely negative, both of which are met for Ti-Fe.<sup>41,44–46</sup> As the sputtering process can be recognized as a rapid cooling event from the vapor to the solid,<sup>47</sup> the intermixing between the layers at such a fine length scale, coupled with system driven to form an intermetallic equilibrium structure,<sup>39</sup> may have simply kinetically constrained

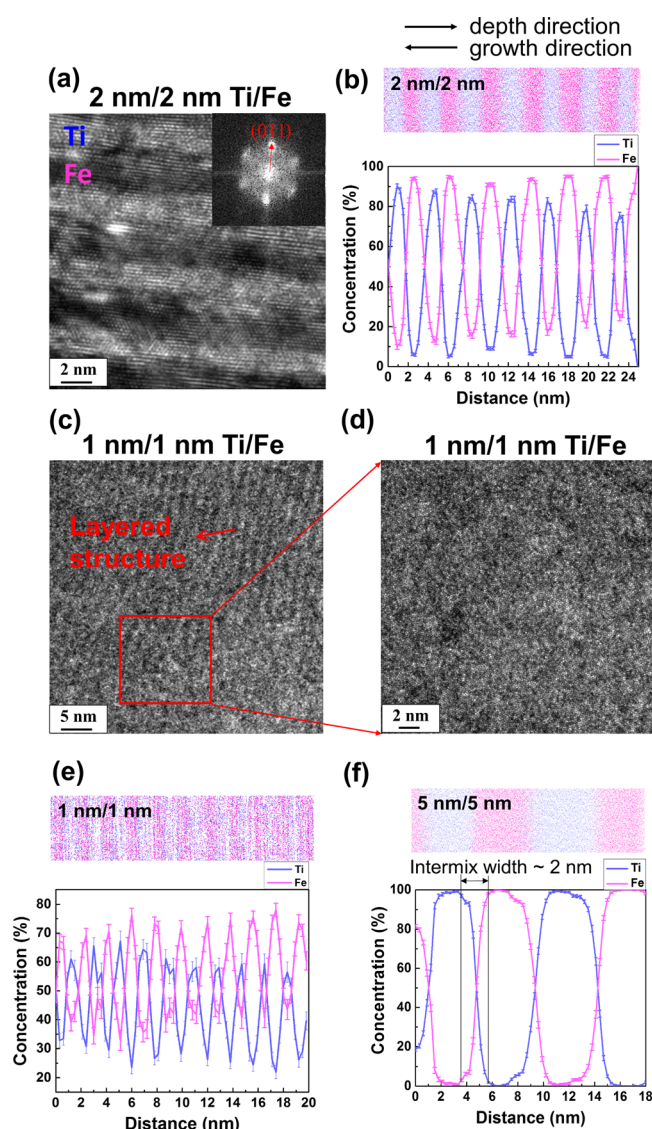


Fig. 3. (Color online) (a) Cross-sectional TEM image of the 2 nm/2 nm Ti/Fe multilayer. The inset is the fast Fourier transformation for this image. It could be seen that the film has a texture of  $\{011\}$  which is in consistent with the out-of-plane texture in the previous XRD result. (b) Atom probe tomography compositional profile of the 2 nm/2 nm film taken along the growth direction. (c) TEM cross-sectional image of the 1 nm/1 nm Ti/Fe multilayer. Some layering structure can still be observed but no crystalline structure was seen. (d) Magnified image from (c). The disordered structure has further supported the observations from the low intensity of this film by the XRD. (e) Atom probe compositional profile of the 1 nm/1 nm multilayer. Intermixing was till observed and more significant than that of the 2 nm/2 nm film. (f) Atom probe compositional profile of the 5 nm/5 nm multilayer. The intermixing width is about 2 nm. This indicated each layer grows continuously once the thickness reaches 1 nm.

the system to become disordered as the adatoms attempted to migrate to their equilibrium lattice sites.

Figure 4(a) is the stress-thickness product plot as a function of film thickness for all the multilayers for the various bilayer thicknesses ranging from 40 to 2 nm. Several observations can be made from the stress plot. First, as the bilayer thickness decreases, the overall stress moves from an overall tensile to compressive state, with a dramatic change between the 5 nm/5 nm and 3 nm/3 nm multilayers. By viewing the stress slopes changes as each layer grows on the other, we can decipher the driving force for these changes. For the thicker bilayers, the Ti layer shows an initial tensile to compressive stress evolution, Fig. 4(b), with the extent of the tensile growth diminishing with reducing

bilayer thickness [Figs. 4(c) and 4(d)]. However, Fe retains a positive or tensile growth behavior regardless of the bilayer spacing. Hence, as the bilayer thickness is reduced, the increasing dominate compressive or negative slope of Ti's growth drives the system to an overall more compressive stress within the multilayer. Once the 3 nm/3 nm film is deposited, the Ti growth shows no initial tensile or positive growth, Fig. 4(e), creating the dramatic increase in compressive stress between it and the 5 nm/5 nm multilayer, Fig. 4(d), which still retains a minor initial tensile growth component. The compressive stress slightly relaxes between the 3 nm/3 nm and the 2 nm/2 nm multilayer [Fig. 4(f)] which is attributed to the change in phase from hcp Ti/bcc Fe to bcc Ti/bcc Fe. Once the film forms the

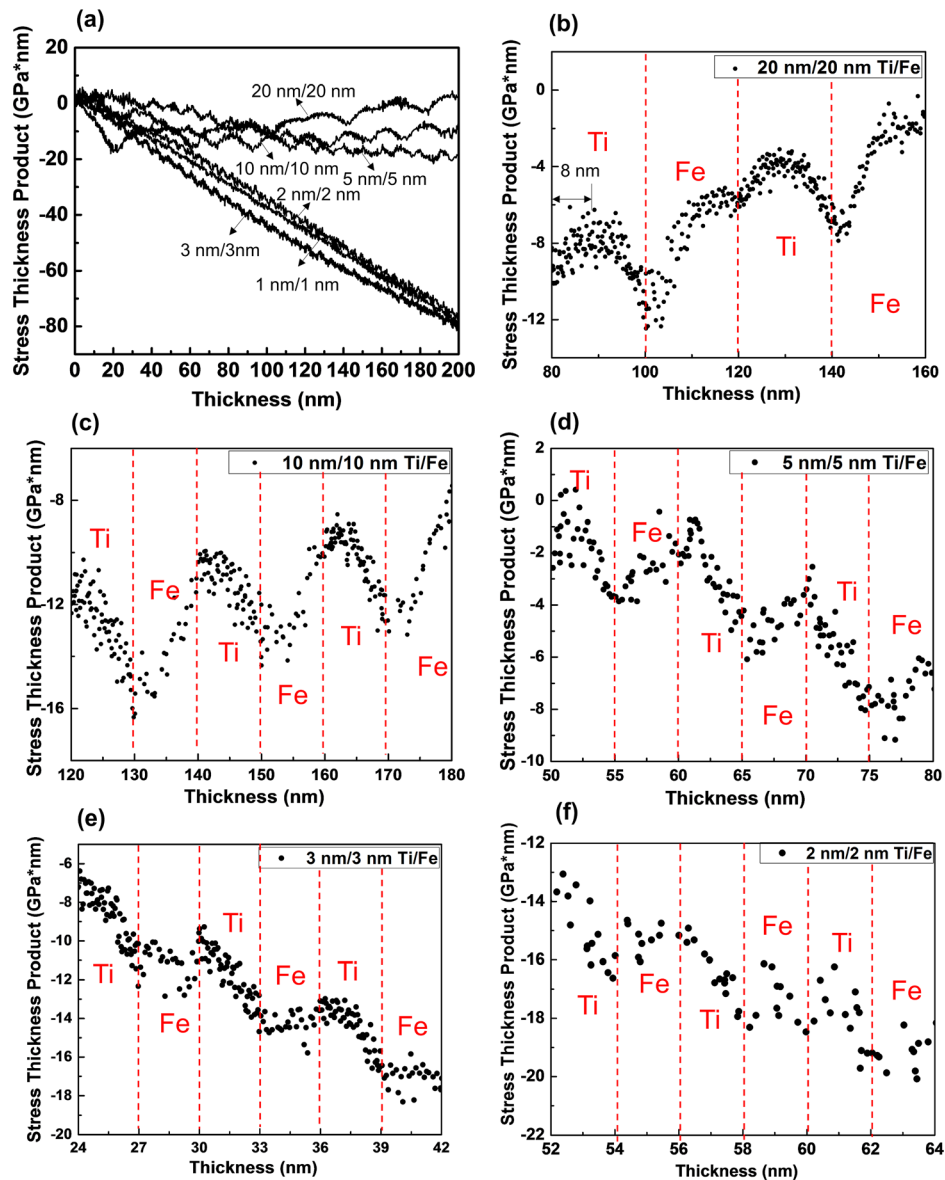


FIG. 4. (Color online) (a) Stress-thickness product plot for Ti/Fe multilayer layers at various layer thicknesses. (b) Magnified stress plot of the 20 nm/20 nm Ti/Fe multilayer. Ti grows tensile up to 8 nm and then rolls back. Fe grows tensile through its whole thickness. (c) Magnified stress plot of the 10 nm/10 nm Ti/Fe multilayer. Ti's tensile growth behavior is not as obvious as that of the 20 nm/20 nm film. (d) Magnified stress plot of the 5 nm/5 nm Ti/Fe multilayer. Ti has a more compressive stress slope than that of the 5 nm/5 nm film and contributes to the large overall compressive stress behavior. (e) Magnified stress plot of the 3 nm/3 nm Ti/Fe multilayer. Ti shows no initial tensile growth behavior. (f) Magnified stress plot of the 2 nm/2 nm Ti/Fe multilayer. The compressive stress slope for Ti slightly relaxes.

amorphous phase, the compressive stress slope value saturates to a value very near the bcc/bcc multilayer's stress.

The prior change in the tensile growth of Ti as a function of bilayer spacing provides an interesting understanding of how Ti is growing on the Fe surface and directly is affected by the layer thickness of the subsurface Fe. For the 20 nm/20 nm multilayer, Ti exhibits a tensile growth behavior up to  $\sim 8$  nm before it rolls over to a negative slope commensurate with a compressive stress. It is clear from this work, that bcc Ti would be very unlikely stabilized to such a layer thickness. Prior work by the authors<sup>18</sup> noted this change over to corresponding with the phase change of the Ti layer. At least in this system, the change in slope is likely more related to the mobility of the adatoms on the growth surface which appear relatively independent of the phase (bcc or hcp) of Ti, if bcc is only stabilized up to  $\sim 2$  nm based on the 2 nm/2 nm multilayer diffraction [Fig. 2(c)]. From the introduction, tensile stresses are associated with either elastic strains of embryonic islands coalescence or low adatom mobility once coalescence has been achieved; in contrast compressive stresses are associated with higher mobility adatoms. Based on prior literature, Ti tends to exhibit postcoalescence compressive growth, while prior literature reports for Fe being a low mobility film that exhibits tensile growth as seen in these multilayers. Thus, it appears that Fe has a much more dramatic influence of Ti's growth (evident by the growth stress variation) as compared to Ti on Fe's growth (which remained relatively consistent and tensile). Using the atom probe compositional profile from the 5 nm/5 nm multilayer, Fig. 3(f), we can determine that the intermixed width for these films is  $\sim 1.5$  to 2 nm and that once a film achieves a thickness  $>1$  nm, the layer itself only contains its own species.

As a comparison of how the different layer thicknesses affect the growth, two nonequivalent layer bilayer multilayers were grown, i.e., a 10 nm Ti/30 nm Fe and a 30 nm Ti/10 nm Fe. The growth stresses and XRD scans/electron diffraction patterns (which confirm both multilayers adopted the bulk phases) are given in Figs. 5(a)–5(d). For the 10 nm Ti/30 nm Fe film, Fig. 5(c), Ti reveals a relatively positive slope growth with the Fe film continuing that trend up to  $\sim 10$  to 15 nm after which the stress is relatively invariant, Fig. 5(a). Upon a closer inspection of the 20 nm/20 nm film, Fig. 4(b), there appears hints of a similar leveling out behavior of the stress near the end of its growth. Ti's lower bulk modulus (110 GPa) than that of Fe (170 GPa)<sup>48</sup> likely contributed to Ti being more compliant to the strains of it growing on the much thicker (rigid) Fe surface. This is manifested by its strain value noted in Table I. According to the interpretation of Shull and Spaepen,<sup>19</sup> as well as others,<sup>23–26</sup> this change in slope would be associated with coalescence of the film on the multilayer growth surface. If this clear variation in slope does represent the point of complete Fe coalescence, then Fe's mobility from one of Volmer–Weber island growth<sup>49</sup> changes to one of near wetting across the surface for thickness  $\geq 10$  to 15 nm. For the 30 nm Ti/10 nm Fe multilayer, the Fe layer maintains a positive slope for all growth conditions and that the Ti exhibits a

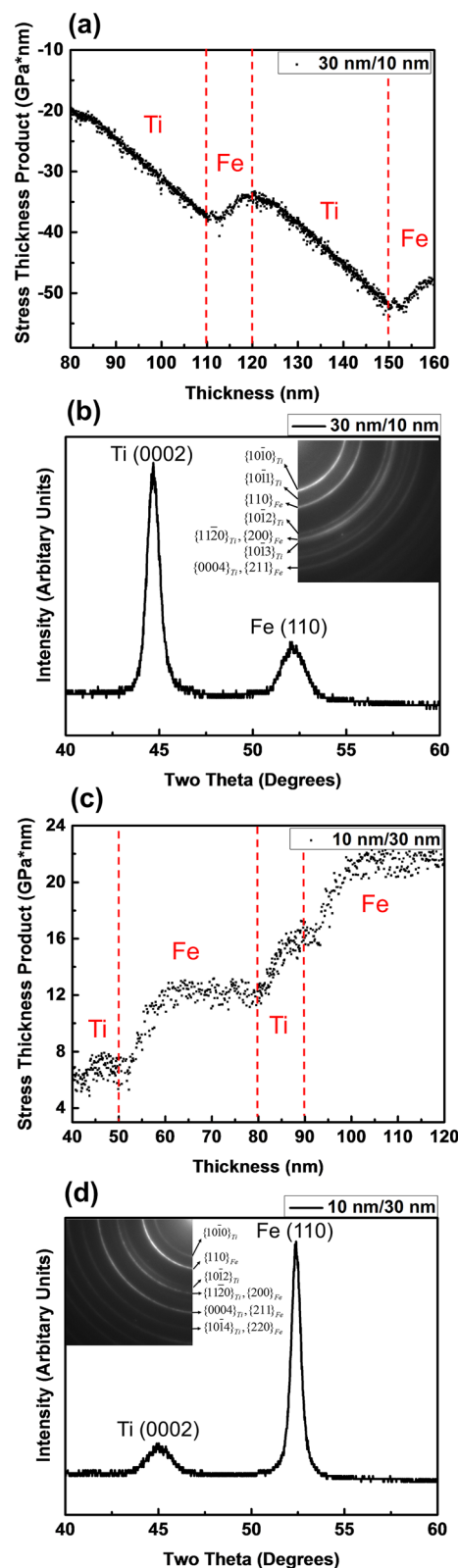


FIG. 5. (Color online) (a) Magnified stress plot for the 30 nm Ti/10 nm Fe multilayer. No significant tensile growth behavior of Ti was observed. The large compressive stress slope of Ti indicates it has considerably good adatom mobility on the Fe surface. (b) XRD scan and electron diffraction pattern taken from the 30 nm Ti/10 nm Fe multilayer confirmed its hcp/bcc structure. (c) Magnified stress plot for the 10 nm Ti/30 nm Fe multilayer. Ti reveals a significant tensile growth which similarly observed in the 20 nm/20 nm film. (d) XRD scan and electron diffraction pattern taken from 10 nm Ti/30 nm Fe multilayer confirmed its hcp/bcc structure.

nearly instantaneous initial compressive growth and never achieves a “leveling out effect” as observed with Fe tensile condition. Thus, even in these nonequivalent bilayers, Fe’s layer thickness continues to influence Ti’s growth stresses. We can conclude that once the Fe layer is sufficiently thin ( $\leq 10$  nm), the Ti layer is driven to grow compressively.

#### IV. SUMMARY

A series of Ti/Fe multilayered thin films with varying bilayer thickness have been sputter-deposited onto [001] Si substrates. As the bilayer thickness was reduced from 40 to 2 nm, the overall stress state changed from tensile to compressive, with the most dramatic change occurring between the 5 nm/5 nm and 3 nm/3 nm. This has been explained by Ti growth stresses on the Fe surface. For bilayers greater than 10 nm, the Ti exhibited a tensile to compressive growth evolution. However, for smaller bilayer spacings, Ti initially grows in a compressive state.

When the multilayer was 2 nm/2 nm, the Ti was stabilized as a bcc phase; however, both the bcc Ti and bcc Fe were highly strained. Further decreases in the bilayer resulted in the vitrification of the multilayer. The crystalline to amorphous phase transitions is attributed to the large atomic size difference, significant intermixing, and negative enthalpy of mixing kinetically constraining the system to form the bulk equilibrium TiFe (or TiFe<sub>2</sub>) intermetallic. These phase changes resulted in a modest reduction of the compressive stress of the film.

#### ACKNOWLEDGMENTS

This work has been supported by the National Science Foundation (Grant No. NSF-DMR-1207220). The authors thank the Central Analytical Facility in the University of Alabama for support.

- <sup>1</sup>T. L. Hylton, K. R. Coffey, M. A. Parker, and J. K. Howard, *Science* **261**, 1021 (1993).
- <sup>2</sup>H. G. Draaisma, W. De Jonge, and F. Den Broeder, *J. Magn. Magn. Mater.* **66**, 351 (1987).
- <sup>3</sup>P. Bhattacharya, R. R. Das, and R. Katiyar, *Appl. Phys. Lett.* **83**, 2010 (2003).
- <sup>4</sup>M. M. D. Kumar and S. Devadason, *Appl. Nanosci.* **3**, 453 (2013).
- <sup>5</sup>D. G. Cahill, A. Bullen, and L. Seung-Min, *High Temp. High Pressure* **32**, 135 (2000).
- <sup>6</sup>Z. Nuru, C. Arendse, T. Muller, S. Khamlich, and M. Maaza, *Sol. Energy Mater. Sol. Cells* **120**, 473 (2014).
- <sup>7</sup>M. Ylilammi and T. Ranta-aho, *Thin Solid Films* **232**, 56 (1993).
- <sup>8</sup>O. S. Heavens, *Optical Properties of Thin Solid Films* (Courier Corporation, North Chelmsford, MA, 1991).
- <sup>9</sup>P. Boher, F. Giron, P. Houdy, P. Beauvillain, C. Chappert, and P. Veillet, *J. Appl. Phys.* **70**, 5507 (1991).

- <sup>10</sup>W. Vavra, D. Barlett, S. Elagoz, C. Uher, and R. Clarke, *Phys. Rev. B* **47**, 5500 (1993).
- <sup>11</sup>G. Thompson, R. Banerjee, S. Dregia, and H. Fraser, *Acta Mater.* **51**, 5285 (2003).
- <sup>12</sup>G. Thompson, R. Banerjee, and H. Fraser, *Appl. Phys. Lett.* **83**, 3471 (2003).
- <sup>13</sup>R. Bruinsma and A. Zangwill, *J. Phys.* **47**, 2055 (1986).
- <sup>14</sup>R. Bruinsma and A. Zangwill, *Europhys. Lett.* **4**, 729 (1987).
- <sup>15</sup>S. Dregia, R. Banerjee, and H. Fraser, *Scr. Mater.* **39**, 217 (1998).
- <sup>16</sup>G. Thompson, R. Banerjee, S. Dregia, M. Miller, and H. Fraser, *J. Mater. Res.* **19**, 707 (2004).
- <sup>17</sup>J. Li, W. Liu, and Q. Jiang, *Acta Mater.* **53**, 1067 (2005).
- <sup>18</sup>L. Wan, X. Yu, and G. B. Thompson, *Acta Mater.* **80**, 490 (2014).
- <sup>19</sup>A. L. Shull and F. Spaepen, *J. Appl. Phys.* **80**, 6243 (1996).
- <sup>20</sup>R. Cammarata, T. Trimble, and D. Srolovitz, *J. Mater. Res.* **15**, 2468 (2000).
- <sup>21</sup>F. Spaepen, *Acta Mater.* **48**, 31 (2000).
- <sup>22</sup>C. Friesen and C. Thompson, *Phys. Rev. Lett.* **89**, 126103 (2002).
- <sup>23</sup>L. Freund and E. Chason, *J. Appl. Phys.* **89**, 4866 (2001).
- <sup>24</sup>J. S. Tello, A. F. Bower, E. Chason, and B. W. Sheldon, *Phys. Rev. Lett.* **98**, 216104 (2007).
- <sup>25</sup>E. Chason, B. Sheldon, L. Freund, J. Floro, and S. Hearne, *Phys. Rev. Lett.* **88**, 156103 (2002).
- <sup>26</sup>J. A. Floro, E. Chason, R. C. Cammarata, and D. J. Srolovitz, *MRS Bull.* **27**, 19 (2002).
- <sup>27</sup>G. Abadias, A. Fillon, J. J. Colin, A. Michel, and C. Jaouen, *Vacuum* **100**, 36 (2014).
- <sup>28</sup>A. González-González, C. Polop, and E. Vasco, *Phys. Rev. Lett.* **110**, 056101 (2013).
- <sup>29</sup>C. Pao, S. M. Foiles, E. B. Webb III, D. J. Srolovitz, and J. A. Floro, *Phys. Rev. Lett.* **99**, 36102 (2007).
- <sup>30</sup>J. W. Shin and E. Chason, *Phys. Rev. Lett.* **103**, 056102 (2009).
- <sup>31</sup>B. Fu, W. An, C. Turner, and G. Thompson, *Phys. Rev. Lett.* **105**, 096101 (2010).
- <sup>32</sup>G. G. Stoney, *Proc. R. Soc. London, Ser. A* **82**, 172 (1909).
- <sup>33</sup>Y. Sasanuma, M. Uchida, K. Okada, K. Yamamoto, Y. Kitano, and A. Ishitani, *Thin Solid Films* **203**, 113 (1991).
- <sup>34</sup>L. Giannuzzi and F. Stevie, *Micron* **30**, 197 (1999).
- <sup>35</sup>K. Thompson, D. Lawrence, D. Larson, J. Olson, T. Kelly, and B. Gorman, *Ultramicroscopy* **107**, 131 (2007).
- <sup>36</sup>D. J. Larson, T. J. Prosa, R. M. Ulfig, B. P. Geiser, and T. F. Kelly, *Local Electrode Atom Probe Tomography* (Springer Science, New York, 2014).
- <sup>37</sup>G. Welsch, R. Boyer, and E. Collings, *Materials Properties Handbook: Titanium Alloys* (ASM International, Materials Park, OH, 1993).
- <sup>38</sup>H. Ledbetter and R. P. Reed, *J. Phys. Chem. Ref. Data* **2**, 531 (1973).
- <sup>39</sup>J. L. Murray, *Bull. Alloy Phase Diagrams* **2**, 320 (1981).
- <sup>40</sup>S. Liou and C. Chien, *J. Appl. Phys.* **55**, 1820 (1984).
- <sup>41</sup>M. Turchanin, A. Abdulov, and P. Agraval, *Russ. Metall.* **2008**, 370.
- <sup>42</sup>A. Fnidiki, J. Juraszek, J. Teillet, N. Duc, T. Danh, M. Kaabouchi, and C. Sella, *J. Appl. Phys.* **84**, 3311 (1998).
- <sup>43</sup>S. Guo and C. T. Liu, *Prog. Nat. Sci.: Mater. Int.* **21**, 433 (2011).
- <sup>44</sup>L. Zaluski, P. Tessier, D. Ryan, C. Doner, A. Zaluska, J. Ström-Olsen, M. Trudeau, and R. Schulz, *J. Mater. Res.* **8**, 3059 (1993).
- <sup>45</sup>T. Mizuno and T. Morozumi, *J. Less-Common Met.* **84**, 237 (1982).
- <sup>46</sup>O. Senkov and D. Miracle, *Mater. Res. Bull.* **36**, 2183 (2001).
- <sup>47</sup>F. Luborsky, *Amorphous Metallic Alloys* (Butterworth and Co, London, UK, 1983).
- <sup>48</sup>“Bulk modulus of the elements,” <http://periodictable.com/Properties/A/BulkModulus.v.html>.
- <sup>49</sup>H. Z. Yu and C. V. Thompson, *Acta Mater.* **67**, 189 (2014).